JGR Solid Earth

RESEARCH ARTICLE
10.1029/2024JB029791

Near-Field Imaging of Near-Identical M_w5.9 Earthquakes in the Crust of Ibaraki, Japan

Keisuke Yoshida[1], **Yo Fukushima**[2], **and Yoshihiro Kaneko**[3]

[1]Research Center for Prediction of Earthquakes and Volcanic Eruptions, Graduate School of Science, Tohoku University, Sendai, Japan, [2]International Research Institute of Disaster Science, Tohoku University, Sendai, Japan, [3]Graduate School of Science, Kyoto University, Kyoto, Japan

Special Collection:
Slow to fast earthquakes and the geology, structure, and rheology of their host subduction zones

Key Points:

- We examined the source processes of two M_w5.9 intraplate earthquakes that produced very similar displacements but different waveforms
- They exhibited distinct rupture processes on the same fault, with their deep slip patches ($3 < z < 6$ km) situated adjacent to each other
- They repeatedly caused seismic slip on the same shallow aseismic segment possibly via dynamic stress changes

Supporting Information:

Supporting Information may be found in the online version of this article.

Correspondence to:

K. Yoshida,
keisuke.yoshida.d7@tohoku.ac.jp

Citation:

Yoshida, K., Fukushima, Y., & Kaneko, Y. (2025). Near-field imaging of near-identical M_w5.9 earthquakes in the crust of Ibaraki, Japan. *Journal of Geophysical Research: Solid Earth*, *130*, e2024JB029791. https://doi.org/10.1029/2024JB029791

Received 26 JUN 2024
Accepted 9 FEB 2025

Author Contributions:

Conceptualization: Keisuke Yoshida, Yo Fukushima
Data curation: Keisuke Yoshida, Yo Fukushima
Investigation: Keisuke Yoshida
Writing – original draft: Keisuke Yoshida
Writing – review & editing: Keisuke Yoshida, Yo Fukushima, Yoshihiro Kaneko

Abstract Understanding the physical mechanisms of intraplate earthquakes requires a better understanding of the earthquake cycle and aseismic slip. A potential short-term repetition of intraplate earthquakes has been documented from interferometric synthetic aperture radar (InSAR) observations of two M_w5.9 events in northern Ibaraki Prefecture, Japan, which occurred on 19 March 2011 and 28 December 2016. However, our understanding based on surface geodetic measurements remains limited, particularly in terms of spatial resolution at depth. Here, we used the near-field seismic waveform data to complement InSAR data, thereby improving the spatial resolution of the coseismic slip distributions. First, we confirmed that the aftershocks of both events occurred along a common fault area. We then conducted a joint inversion that successfully reconciled near-identical surface displacements with the different seismic waveforms. Our results indicate that while the 2011 event mainly ruptured just updip of the hypocenter at 6 km depth, the 2016 rupture initiated deeper, at 10 km, and propagated to the shallow, northern side, causing large slip near the 2011 rupture area. The slip distributions of two events were complementary in the deeper portion ($3 < z < 6$ km), whereas those on the shallower side ($z < 3$ km) largely overlapped, resulting in nearly identical surface displacements. Small earthquakes rarely occur shallower than 3 km, suggesting that this shallow segment releases accumulated strain aseismically. The two events repeatedly triggered seismic slip on this typically aseismic shallow segment, possibly due to dynamic stress changes.

Plain Language Summary Two M_w5.9 crustal earthquakes occurred in northern Ibaraki Prefecture, Japan, in 2011 and 2016, resulting in very similar surface displacements. While previous geodetic studies have suggested that these two events represent a rare instance of extremely short-term earthquake repetition on an intraplate fault, slip at depth may not have been fully resolved by geodetic data alone. In this study, we used near-field seismic waveform data to complement existing geodetic data and improve the spatial resolution of coseismic slip distributions. First, we confirmed that the aftershocks of both events occurred along a common planar structure. We then combined near-field seismic waveform and surface displacement data to estimate fault slip evolution. The results revealed that the two events ruptured slightly different fault sections at greater depths ($3 < z < 6$ km) with distinct rupture characteristics. However, the shallowest parts of the fault ($z < 3$ km) experienced repeated slip on nearly identical slip areas, producing strikingly similar surface displacement patterns. Small earthquakes rarely occur at such shallow depths, suggesting that this shallow segment releases accumulated strain aseismically. Due to dynamic stress changes, however, the two mainshocks may have caused seismic slip on this otherwise aseismic segment, resulting in characteristic surface displacements.

1. Introduction

Understanding earthquake occurrence processes requires understanding the stress accumulation and release processes in seismogenic regions. At plate boundaries, a common view is that aseismic slip loads seismic patches (asperities) and generates earthquakes (Lay & Kanamori, 1981). An increase in strain and stress on fault is monitored via geodetic analysis (Saito & Noda, 2022; Savage, 1983), which exhibits substantial lateral variations (e.g., Noda et al., 2018; Ryder & Bürgmann, 2008; Suwa et al., 2006). This depiction typically applies to plate-boundary faults, while it remains unclear whether this applies to intraplate faults. For intraplate faults, the frictional and rheological properties, fault maturity, loading rate, and the cause of loading may differ significantly from those of interplate faults.

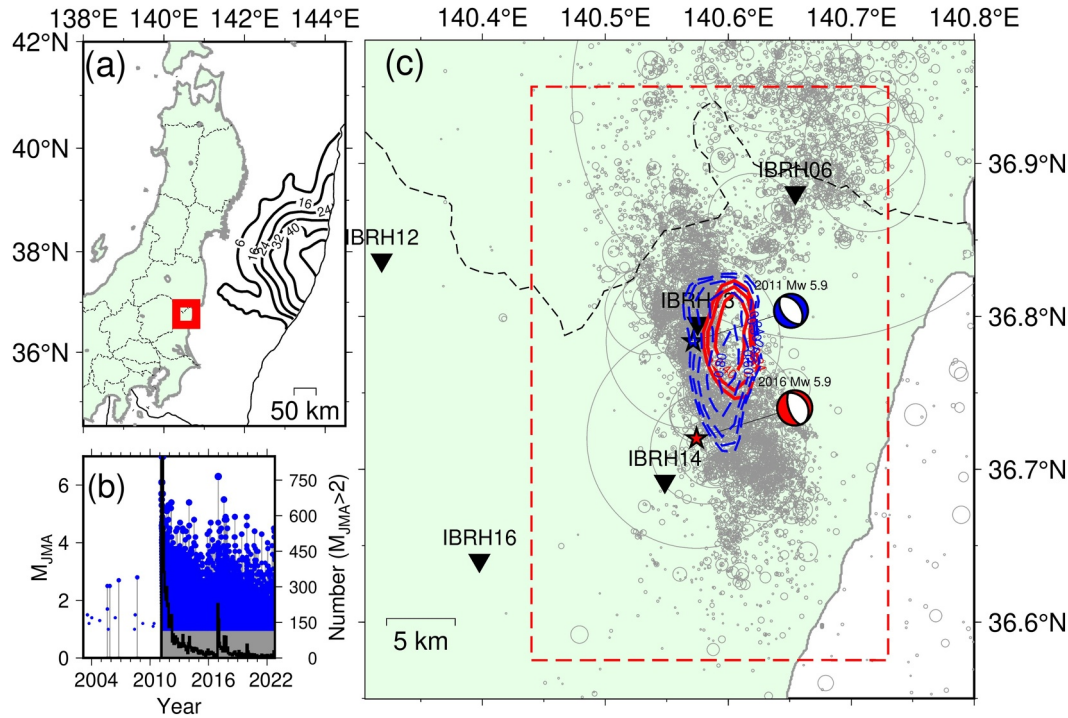

Figure 1. (a) Map showing the study region. Red rectangle indicates the area shown in (c). Black contour lines show the coseismic slip distribution of the 2011 M9 Tohoku event (Kubota et al., 2022). (b) Magnitude–time diagrams in the study region. Blue circles with gray bars indicate the magnitudes in the Japan Meteorological Agency unified catalog. The black line denotes the number of earthquakes with $M_{JMA} \geq 2.0$, which is well beyond the lower detection limit. (c) Hypocenter distribution. Gray circles show the hypocenters of shallow earthquakes ($z < 40$ km) with $M_{JMA} \geq 2.0$ from 1 January 2003 to 30 September 2022. The circle sizes correspond to the diameters of Eshelby's (1957) circular fault with a stress drop of 3 MPa. Stars and beach balls show the hypocenters and moment tensors for the two events, with blue and red indicating the 2011 and 2016 M_w5.9 events, respectively. Black triangles denote the stations whose waveforms are shown in Figure 3. Blue and red contour lines represent the coseismic slip distributions for the 2011 and 2016 events, respectively, by Fukushima et al. (2018).

Island arc crusts in subduction zones have various faults away from plate boundaries, each generating earthquakes. The force exerted on the plate boundary is the primary cause of stress fields that drive intraplate deformation. Consequently, shallow intraplate faults have significantly lower loading rates than plate-boundary faults. Aseismic deformation on the deep extension may cause stress concentrations away from the plate boundary (Iio & Kobayashi, 2002). While some cases of interseismic aseismic deformation have been documented for shallow intraplate faults (e.g., Meneses-Gutierrez & Nishimura, 2020), such observations remain limited owing to their long recurrence intervals.

An important rationale supporting the asperity model is the existence of repeating earthquakes that rupture the same fault area (Matsuzawa et al., 2002; Nadeau & Johnson, 1998; Uchida & Bürgmann, 2019). They are interpreted as occurring in persistent asperities on faults surrounded by aseismic areas, and their detection is often based on the high similarity of seismic waveforms (e.g., Uchida & Bürgmann, 2019). Recently, repeating earthquakes have also been detected on intraplate faults far from the plate boundaries (Bourouis & Bernard, 2007; Hayashi & Hiramatsu, 2013; Hiramatsu et al., 2011; Lengliné et al., 2014; Lin et al., 2016; Nakajima & Hasegawa, 2023; Naoi et al., 2015; Yoshida, Hasegawa, et al., 2020; Yoshida, Taira, et al., 2020; Yukutake et al., 2022), suggesting that earthquakes on intraplate faults also occur at asperities on the faults, and the surrounding aseismic slip contributes to stress accumulation. However, most intraplate repeating earthquakes detected in previous studies were small ($M_w < 4$), and their details, including the validity of their detection, have not been thoroughly examined.

In the northern Ibaraki Prefecture region of Japan, the seismicity level of normal-fault earthquakes drastically increased after the 2011 M9 Tohoku event (Figures 1a and 1b, and Figure S1 in Supporting Information S1). In this region, a normal fault stress regime under east-west tension had locally developed before the Tohoku

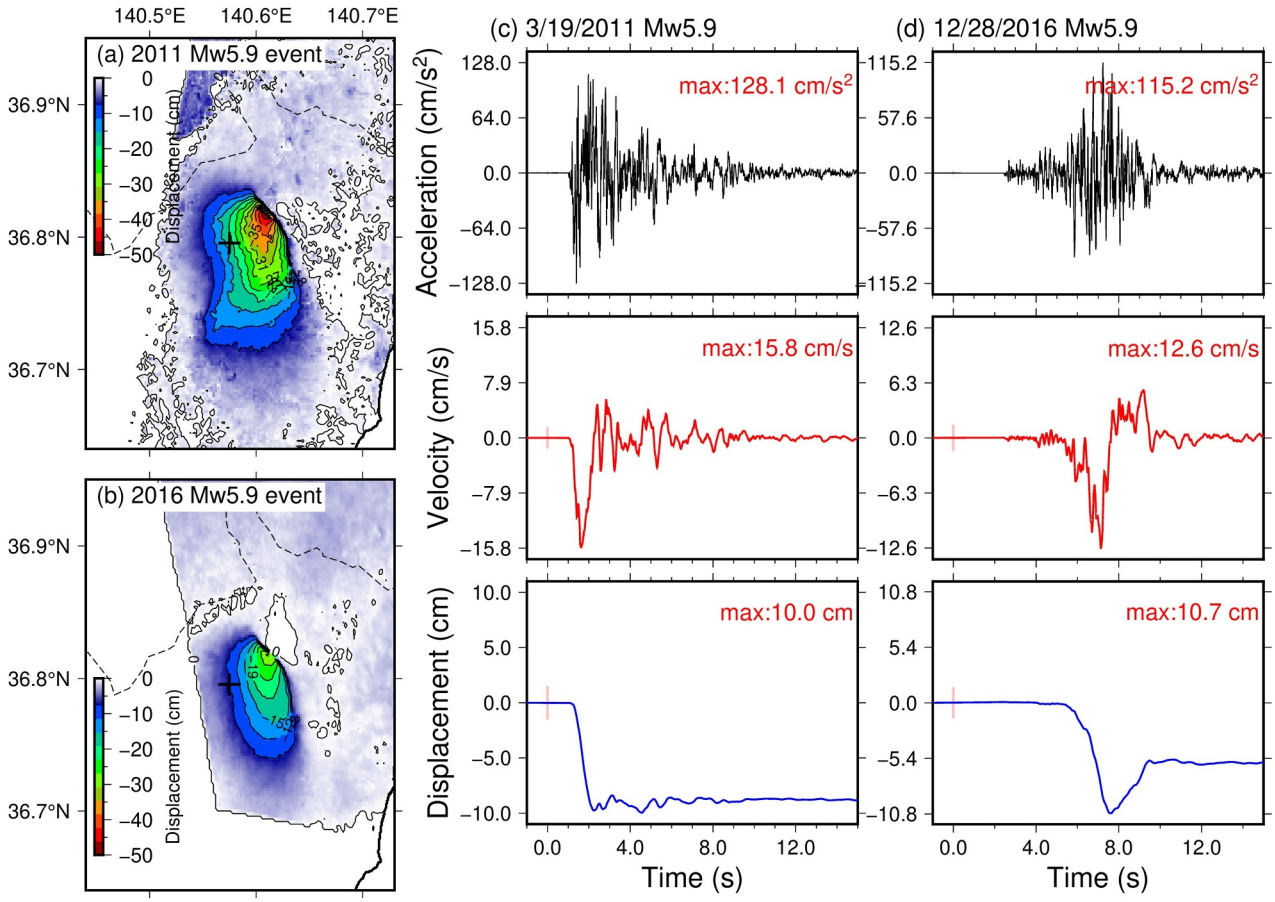

Figure 2. Interferometric synthetic aperture radar (InSAR) records and seismic waveforms (vertical component) during the 2011 and 2016 M_w5.9 events at the IBRH13 downhole accelerometer. (a) and (b): Quasi-vertical components from InSAR records for the 2011 and 2016 events, respectively, by Fukushima et al. (2018). The cross indicates the location of station. (c) and (d): Vertical components of acceleration, velocity, and displacement seismic waveforms for the 2011 and 2016 events, respectively.

earthquake, which is an unusual feature for northeastern Japan (Imanishi et al., 2012; Yoshida et al., 2015a). Before the Tohoku earthquake, the stress rate was low or even negative, primarily due to east-west compression resulting from the slip deficit at the plate boundary. However, following the Tohoku earthquake, the loading rate increased significantly due to the coseismic slip and subsequent afterslip (Imanishi et al., 2012; Kato et al., 2011; Yoshida et al., 2012, 2015a, 2019), which led to the drastic increase in seismicity. Magen et al. (2024) suggest that creep on an offshore shallow normal fault also contributed to loading this area for up to a month after the Tohoku earthquake.

Unusually similar crustal deformations were observed associated with two M_w5.9 earthquakes 5.8 years apart in 2011 and 2016 (Figure 1). The first event was an M_w5.87 earthquake on 19 March 2011, and the second was an M_w5.94 earthquake on 28 December 2016. Here, the moment magnitudes, M_w, were based on the results of the W-phase inversion by Kanamori et al. (2020). The Interferometric synthetic aperture radar (InSAR) observation provided very similar surface displacements associated with the two events (Figures 2a and 2b; Fukushima et al., 2018). Fukushima et al. (2018) inferred that the 2011 and 2016 M_w5.9 events ruptured the same area on an identical fault. Subsequent studies examined the evolution of deformation as well as stress and strain changes in this region by using InSAR and GNSS data (Magen et al., 2024; Wimpenny et al., 2022). According to Wimpenny et al. (2022), the coseismic slip during the Tohoku earthquake induced approximately 10 microstrain of E–W stretching in the region. This was followed by an additional ~0.4 microstrain of E–W stretching between 11 March and 18 March, just prior to the 2011 M_w5.9 event. During the interevent period between these two M_w5.9 events, the GPS network recorded 3.1–3.6 microstrain. Wimpenny et al. (2022) conducted quantitative modeling of the surface displacement and stress field, concluding that the repetition of these events required reduced fault

strength. Since the GNSS stations are located outside the source region, it remains challenging to accurately determine the spatio-temporal variations in stresses on the fault using GNSS data.

A key indication in previous geodetic studies has been that the two events repeatedly ruptured the same fault segment. However, the seismic waveform inversion results provide a significantly different picture of these earthquakes. Tanaka and Iwakiri (2017) and Hikima (2023) reported that the slip areas of the two events based on seismic waveform modeling are not the same but rather located complementarily. However, their widely different slip models do not explain the near-identical surface displacements obtained from the InSAR observations (Figure 3 of Hikima, 2023). Hikima (2023) suggested that in addition to the 2011 coseismic slip, further slip is necessary to explain the observed amount of surface displacement, with a possible candidate being an early afterslip within a day of the mainshock. Based on the analysis of GNSS data from 12 March to 10 April 2011, Magen et al. (2024) also identified significant slip on the fault of the 19 March 2011 earthquake that was not associated with coseismic slip, suggesting the occurrence of pre-and/or postseismic slip.

Determining whether the surface displacement immediately after an earthquake is primarily caused by coseismic slip or is strongly affected by other effects (e.g., early afterslip or slow plastic deformation) is critical for understanding the fault dynamics. However, previous studies analyzed the seismic and geodetic data separately and did not investigate whether the two data sets could be explained by common coseismic slip models. Given the nonuniqueness of inversion solutions, joint inversion is needed to better resolve rupture processes (Dreger et al., 2015; Funning et al., 2014; Kim et al., 2016; Kubo et al., 2013; Wald & Heaton, 1994; Yoshida et al., 1996). Moreover, this pair of earthquakes provides a rare opportunity to study the possible repetition of nearly M_w6 intraplate earthquakes using near-field observations (the closest seismic station is 1.4 km from the epicenter), which can provide critical insights into intraplate processes. In this study, we investigated the fault structures, rupture processes, and slip distributions of the two M_w5.9 events using the hypocenter distribution, near-field seismic waveform data, and geodetic data.

2. Near-Field Seismic Waveforms

Fortunately, two downhole strong-motion sensors (IBRH13 and IBRH14 in Figure 1c) were located close to the epicenters of the two events and recorded high-quality accelerations (Figures 2c and 2d and Figure S2 in Supporting Information S1; Yoshida, 2024). According to information from the National Research Institute for Earth Science and Disaster Resilience (NIED) Hi-net, downhole sensors are surrounded by granite with high seismic velocities (https://www.hinet.bosai.go.jp/st_info/detail/?LANG=en). Figures 2c and 2d show the velocity and displacement waveforms (vertical components) obtained by performing one and two integrations on the acceleration waveforms from the downhole sensor of station IBRH13. We observed the velocity pulses and static displacements associated with these two events. Figures 2a and 2b show the quasi-vertical displacements (tilted 8.4° south of the vertical) estimated by Fukushima et al. (2018) by converting line-of-sight (LOS) displacements from two different directions. Based on the KiK-net data, the final vertical displacement was approximately 10 cm for the 2011 event, whereas it was approximately 6 cm for the 2016 event. These vertical displacement values are slightly smaller than the InSAR quasi-vertical observations (17.2 cm for the 2011 event and 7.8 cm for the 2016 event). This may be attributed to several factors, including postseismic deformation in the InSAR data (the conversion includes data obtained approximately 1 month after each event) and the tilt.

The waveform characteristics of the two events exhibit distinct differences. Figure 3 compares the vertical velocity waveforms with and without a 0.25 Hz low-pass filter. The cutoff frequency corresponds to the approximate S-wave corner frequency of an M_w5.9 event with a stress drop of 3 MPa based on the Brune (1970) source model. This frequency is comparable to the recommended upper limit of the frequency band to detect repeating earthquakes of this size (Uchida, 2019). After filtering, the waveforms still retain their different characteristics that are less evident at teleseismic distances (Wimpenny et al., 2022), highlighting the importance of using near-source data.

3. Fault Structure and Aftershocks

We examined the fault structures and early aftershocks of the two M_w5.9 events. The hypocenters were obtained from Yoshida et al. (2024a, 2024b), who refined the one-dimensional velocity model in this region and relocated the hypocenters of 33,400 $M_{JMA} > 1$ events using near-source observational data. The standard errors for the 2011 hypocenter are 0.23 km in longitude, 0.17 km in latitude, and 0.22 km in depth. For the 2016 hypocenter, the standard errors are 0.26 km in longitude, 0.14 km in latitude, and 0.24 km in depth.

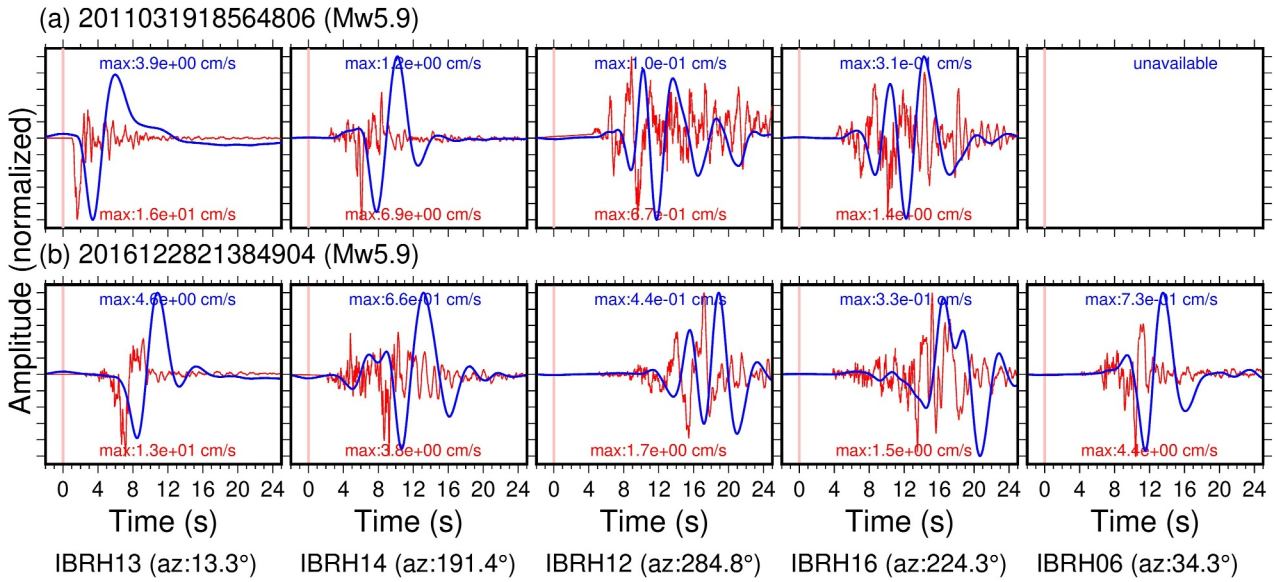

Figure 3. Velocity waveforms of the transverse S-waves of the (a) 2011 and (b) 2016 M_w5.9 events at the five stations shown in Figure 1c. Blue and red show the waveform with and without a low-pass filter with a cutoff frequency of 0.3 Hz. The time at $t = 0$ corresponds to the origin time.

Figures 4 and 5 show maps and cross-sectional views of the hypocenters, respectively. The aftershocks within a week of the 2011 and 2016 M_w5.9 events are shown in Figures 4a and 4b, respectively. Most events are concentrated at depths of 3–11 km, with only a few occurring at depths shallower than 3 km. The distribution near

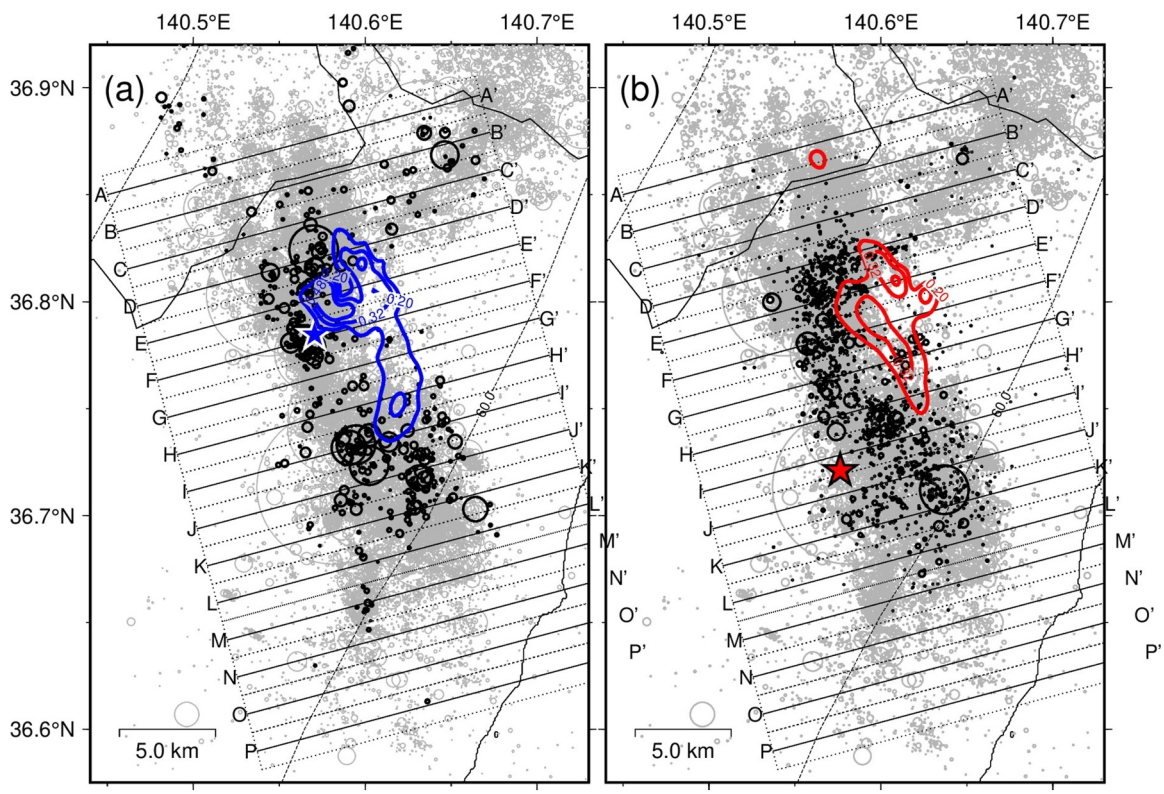

Figure 4. Hypocenter distributions. Black circles represent aftershocks within a week of the (a) 2011 and (b) 2016 M_w5.9 events. Circle sizes correspond to the fault diameter, assuming a stress drop of 3 MPa. Blue and red stars represent the epicenters of the 2011 and 2016 M_w5.9 events, respectively. The contour lines indicate the mainshock coseismic slip distributions.

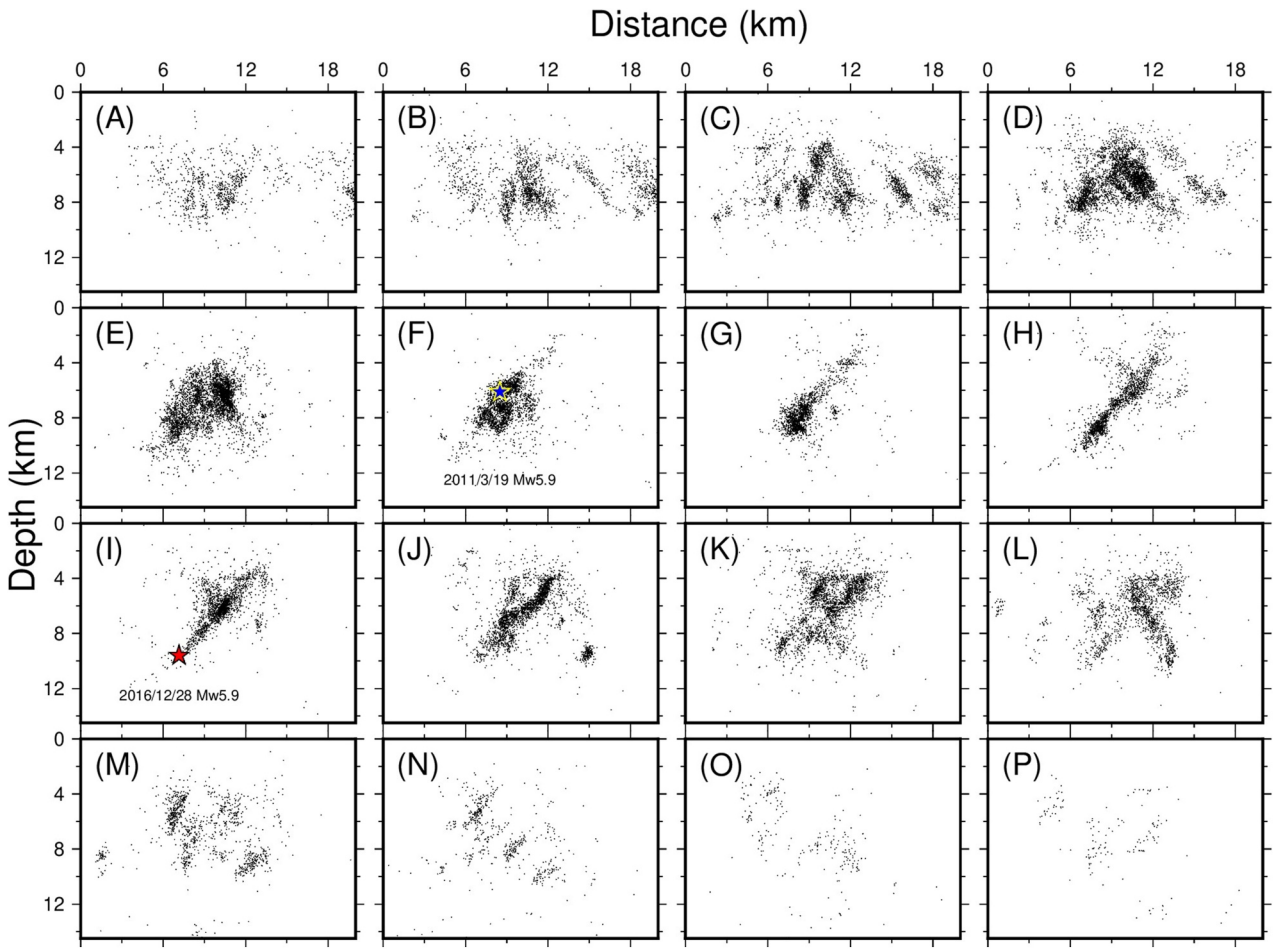

Figure 5. Cross-sectional view of the hypocenters. The 16 subfigures show across-fault vertical cross-sections along the lines shown in Figure 4. Blue and red stars indicate the hypocenters of the 2011 M_w5.9 and 2016 M_w5.9 events, respectively.

the northern (Figures 5a–5d) and southern edges (Figures 5k–5p) is complex, showing an intricate distribution of multiple conjugate planar structures. However, a large west-dipping planar structure is observed in the central region between the two hypocenters (Figures 5g–5j).

Previous studies have suggested that this west-dipping planar structure represents the fault of the 2011 M_w5.9 event (Yoshida et al., 2015b). Figure 6 shows the focal mechanisms of the F-net moment tensor catalog (Kubo et al., 2002) at the hypocenters. The focal mechanisms of these two M_w5.9 events and other events were consistent with the west-dipping plane and several conjugate planes. The 2016 M_w5.9 event likely produced a rupture on this plane. Figures 4 and 7 show the distribution of $M_{JMA} \geq 2$ aftershocks within a week of each M_w5.9 event. They are distributed on the same west-dipping planar structure in the central part, with similar lateral ranges.

However, the rupture initiation points (hypocenters) of the two events are distinct: the 2011 M_w5.9 event initiated at the middle depth of this planar structure ($z = 6.1$ km; Figure 7b), while the 2016 M_w5.9 event started from a southern and deeper position ($z = 9.6$ km; Figure 7d). The distance between the two hypocenters is approximately 10 km. The large differences in the hypocenter locations indicate that their rupture processes widely differed.

4. Coseismic Slip Distributions for the Two M_w5.9 Events

4.1. Data

We estimated the rupture processes of the two M_w5.9 events using joint inversion of near-source waveform and InSAR data (Figure 2). The InSAR records from Fukushima et al. (2018) were included in our data set (Figures 8a and 8d), with the long-wavelength displacement signals caused by the Tohoku earthquake already removed. Each

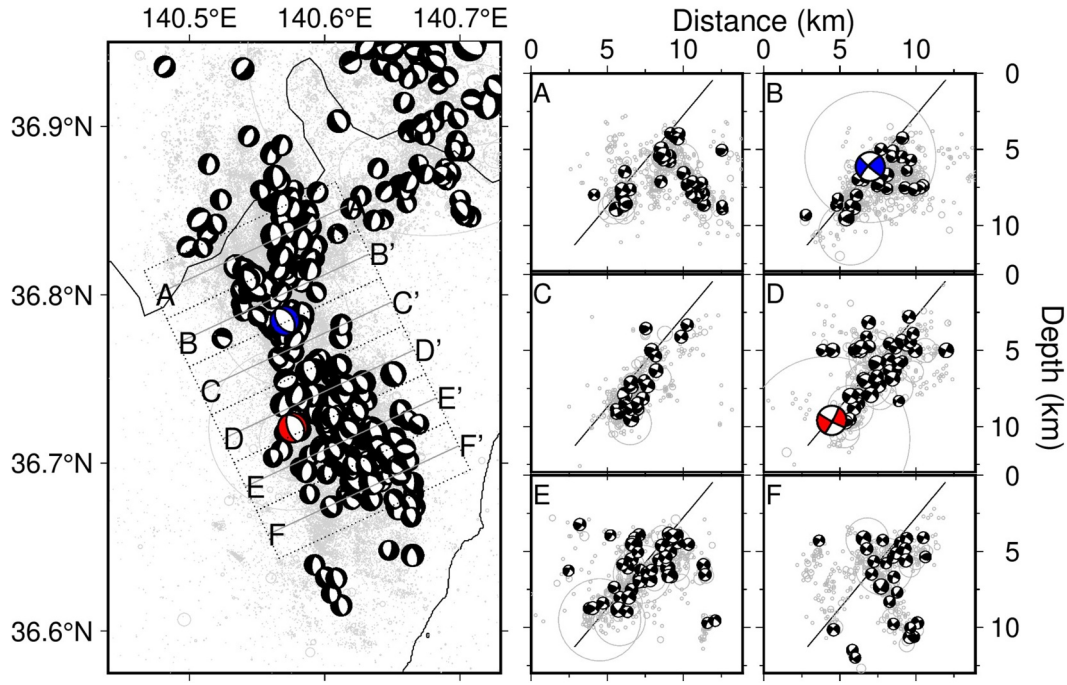

Figure 6. Distribution of the focal mechanisms from the F-net catalog. Blue and red represent the 2011 and 2016 M_w5.9 events, respectively. Gray circles indicate the hypocenters. (a)–(f): Cross sections indicated in the map to the left; the black lines represent the model fault.

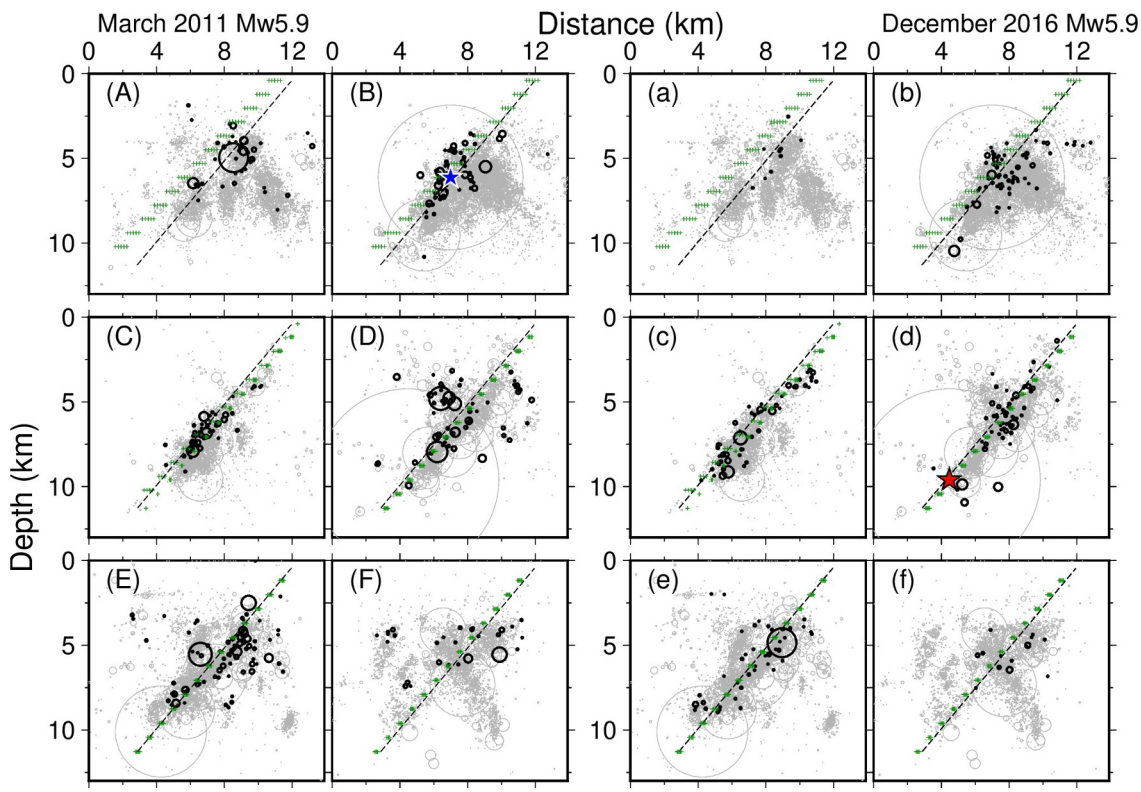

Figure 7. Distribution of early aftershocks within a week of the 2011 and 2016 M_w5.9 events. Locations of cross-sections are shown in Figure 6a. Black circles show aftershocks within a week, and gray ones show all events. (a)–(f): The 2011 M_w5.9 event, and (a)–(f): the 2016 M_w5.9 event. The stars represent the mainshocks. The broken lines represent the model fault. The green crosses indicate the locations of the subfaults of the two-fault model.

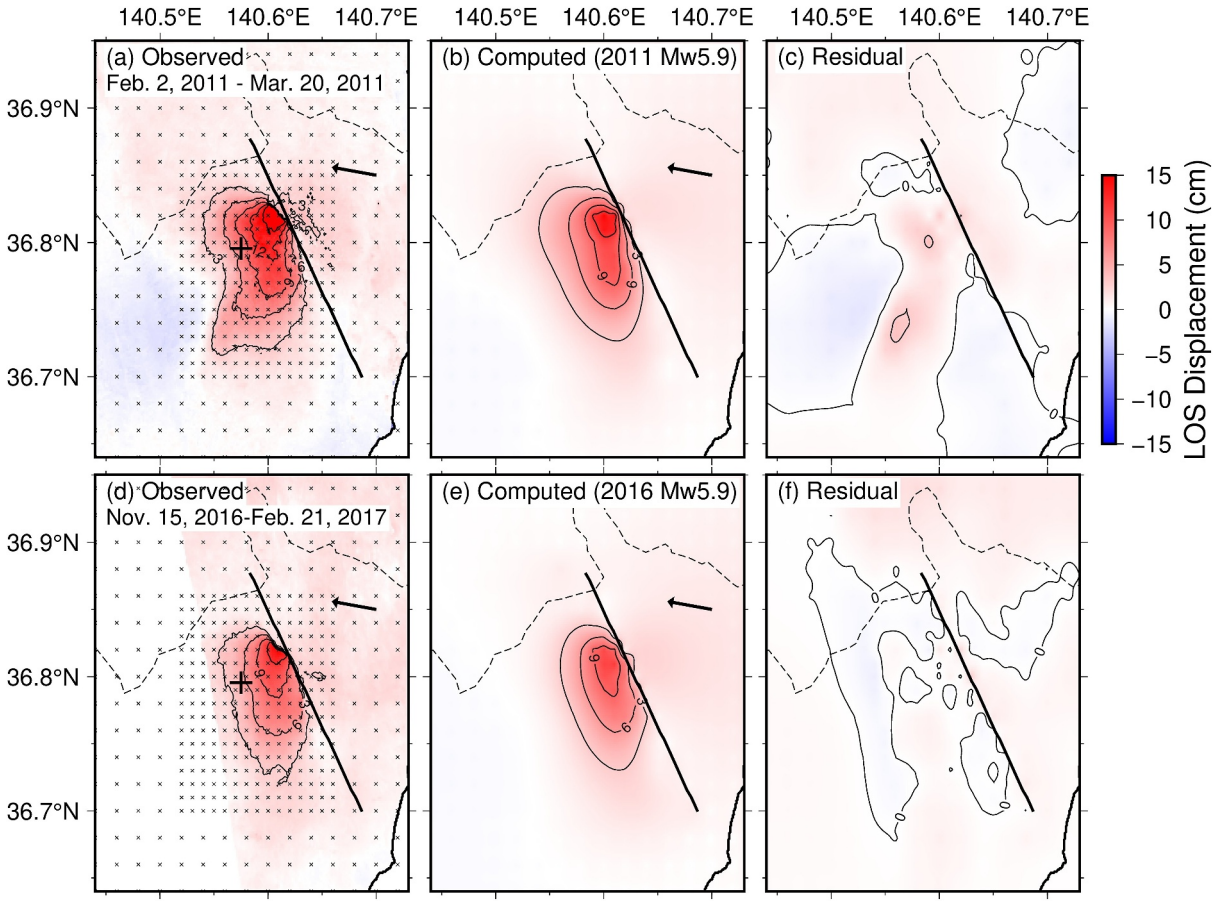

Figure 8. Observed and computed surface displacements in the line-of-sight (LOS) directions associated with the 2011 and 2016 M_w5.9 events. The arrows indicate the LOS direction. (a) and (d): Surface displacements after the 2011 and 2016 M_w5.9 events, respectively, obtained from interferometric synthetic aperture radar observations. (b) and (e): Surface displacements calculated from the slip distributions obtained in this study (Figure 9) for the 2011 and 2016 M_w5.9 events, respectively. (c) and (f): Observed-minus-computed (O–C) residuals for the 2011 and 2016 M_w5.9 events, respectively.

interferogram was obtained from the images acquired before and after the earthquake: 27 days prior and one day after for the 2011 event, and 44 days prior and 56 days after for the 2016 event. The LOS directions are in the ENE direction (azimuth of 280.32°, indicated by the arrows in Figure 8) both for the 2011 and 2016 events (incidence angle of 38.7° and 36.2°, respectively). Additionally, we used seismic waveform records obtained from five downhole sensors at KiK-net stations within 20 km of the hypocenters (Figure 1c). Unfortunately, because the waveform was not recorded at one station (IBRH06) at the time of the 2011 event, we used only waveforms from the other four stations for this event. We used all the three components in our inversion.

The InSAR data were downsampled at 0.01° intervals in areas of high displacement and at 0.02° intervals in areas of low displacement, as indicated by the crosses in Figures 8a and 8d. The high-cut frequency for seismic waveform was set at 1 Hz and downsampled at 0.1 s intervals. The velocity waveforms obtained by integrating the acceleration waveforms were used.

4.2. Method

We retrieved time-dependent slip distributions using the methods of Hartzell and Heaton (1983) and Wald and Heaton (1994), by simultaneously inverting the InSAR and waveform data. It was assumed that the rupture front propagates along the model fault at a constant velocity V_r from the hypocenter. The model fault was set based on the aftershock distribution and focal mechanisms, as shown in Figures 6 and 7. We used a common geometry of the subfaults for these two events. The strike angle is 155°, and the dip angle is 50°, with a length of 22.5 km and a width of 9.9 km. The hypocenters of the two events were located at the center of different subfaults. We allowed the rake angle to vary within a range of −90° to ±45° for each subfault and time window. The model fault was

divided into 408 subfaults, with a length of 0.66 km and width of 1.28 km. The number of subfaults was 34 along the fault length and 12 along the fault width. The shallowest subfault center is 0.47 km deep, and the deepest subfault center is 11.2 km deep. The local moment rate function at each subfault was represented by the superposition of five triangular submoment-rate functions (sMRFs) with a half-duration of t_h. At each subfault, the onset of the ith sMRF occurs at $t = t_{\mathrm{front}} + (i-1)t_{\mathrm{h}}$, where t_{front} is the time when the rupture front reaches the center.

We estimated a vector $\boldsymbol{m}$ containing the amplitudes of 2040 (408×5) sMRFs by solving the following linear equation:

$$W\boldsymbol{d}_{\mathrm{obs}} = WG\boldsymbol{m}. \tag{1}$$

where $\boldsymbol{d}_{\mathrm{obs}} = \begin{pmatrix} \boldsymbol{d}_{\mathrm{wv}}/\mathrm{SSR}_{\mathrm{wv}} \\ \boldsymbol{d}_{\mathrm{InSAR}}/\mathrm{SSR}_{\mathrm{InSAR}} \end{pmatrix}$ is the data vector containing the amplitudes of the waveforms ($\boldsymbol{d}_{\mathrm{wv}}$) and InSAR data ($\boldsymbol{d}_{\mathrm{InSAR}}$), G is the synthetic waveform matrix, and W is a diagonal matrix to weight each equation. We normalized $\boldsymbol{d}_{\mathrm{wv}}$ and $\boldsymbol{d}_{\mathrm{InSAR}}$ in $\boldsymbol{d}_{\mathrm{obs}}$ as well as the corresponding synthetics in G using their sums of square root ($\mathrm{SSR}_{\mathrm{wv}}$ and $\mathrm{SSR}_{\mathrm{InSAR}}$, respectively). As components of the diagonal matrix W, we set the weights of the waveform data to a constant value of 1 and the relative weights of the InSAR data to r_{wt}, where r_{wt} is determined later. To obtain the synthetic waveform and displacement data (G), we used the wavenumber integration code of Zhu and Rivera (2002) and the depth-dependent medium model of Yoshida et al. (2024a) (Figure S3 in Supporting Information S1) based on the empirical relationship with seismic velocity.

We used the nonnegative least-squares algorithm of Lawson and Hanson (1995) to obtain m under damping conditions. We determined the specific damping factor of $\lambda = 0.4$ based on the trade-off curve. Since the residuals increase rapidly when λ exceeds this point, the current setting produces a slip distribution near the resolution limit. The slip distribution was computed from the moment-release distributions obtained with depth-dependent rigidity. Then, we performed joint inversion under various V_r/V_s (0.1–0.9 at 0.1 intervals), t_h (0.1–1.2 s at 0.1 s intervals), and r_{wt} (0.5, 1.0, and 2.0). Here, V_s is the S-wave velocity at the depth of the respective hypocenter, which is 3.45 and 3.52 km/s for the 2011 and 2016 events, respectively.

We computed the variance reduction, $\mathrm{VR} = 100 \times \left(1 - \frac{\sum (d_i - s_i)^2}{\sum d_i^2}\right)$, between the synthetic (s_i) and observed amplitudes (d_i) for the seismic waveform ($\mathrm{VR}_{\mathrm{wv}}$) and InSAR data sets ($\mathrm{VR}_{\mathrm{InSAR}}$), respectively. We adopted $r_{\mathrm{wt}} = 1.0$, which maximizes the average variance reduction, $\mathrm{VR}_{\mathrm{mean}} = (\mathrm{VR}_{\mathrm{wv}} + \mathrm{VR}_{\mathrm{InSAR}})/2$, to account for both data sets.

4.3. Results

The optimal parameters are $V_r/V_s = 0.9$ and $t_h = 0.2$ s for the 2011 event and $V_r/V_s = 0.6$ and $t_h = 0.4$ s for the 2016 event. Figures 9a and 9b show the derived coseismic slip distributions for the 2011 and 2016 events. The slip distribution in the fault coordinates, and the waveform fitting are shown in Figure S3 in Supporting Information S1. Our models reconcile the observations of near-identical surface displacements (Figures 8b, 8c, 8e, and 8f) with differing seismic waveform data (Figure S3 in Supporting Information S1). $\mathrm{VR}_{\mathrm{mean}}$ is 88.4% ($\mathrm{VR}_{\mathrm{wv}}$ is 83.9% and $\mathrm{VR}_{\mathrm{InSAR}}$ is 92.9%) for the 2011 event and 89.3% ($\mathrm{VR}_{\mathrm{wv}}$ is 86.2% and $\mathrm{VR}_{\mathrm{InSAR}}$ is 92.5%) for the 2016 event. In both events, $\mathrm{VR}_{\mathrm{InSAR}}$ shows high values (>80%) with little dependence on the assumed V_r or t_h, whereas $\mathrm{VR}_{\mathrm{wv}}$ shows a strong dependence on them (Figure S4 in Supporting Information S1).

The estimated M_{w} is 5.92 for the 2011 event and 5.88 for the 2016 event, similar to the estimates based on W-phase inversion (Kanamori et al., 2020). In both events, the estimated rake angles were consistent with normal fault slip for each subfault (Figure S3 in Supporting Information S1). We calculated the distribution of the shear stress change on the fault based on Okada (1992) for a semi-infinite elastic body (Young's modulus of 80 GPa and Poisson's ratio of 0.25). The energy-based stress drop (Noda et al., 2013) is $\Delta\sigma_E = 1.4$ MPa for the 2011 event and 0.9 MPa for the 2016 event (Figure S5 in Supporting Information S1). The stress drop around the slip peak exceeded 5 MPa for the 2011 event. According to Kanamori et al. (2020), the radiated energies of the 2011 and 2016 events are $E_R = 1.5 \times 10^{13}$ and 9.9×10^{12} J, respectively. The 2011 earthquake exhibited a larger maximum slip, stress drop, rupture velocity, radiated energy, and slightly greater seismic moment, contributing to

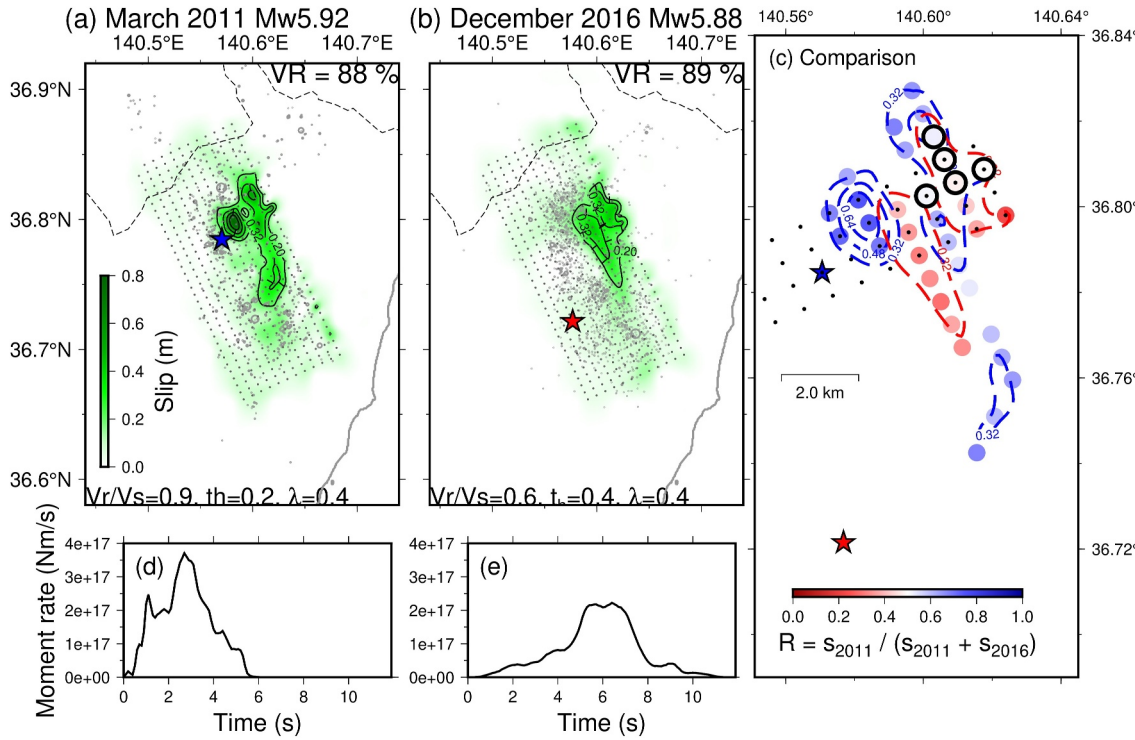

Figure 9. Coseismic slip distributions for the (a) 2011 and (b) 2016 M_w5.9 events obtained via joint inversion. The contour lines indicate the slip amount. The stars denote the mainshock hypocenters. Gray circles show aftershocks within 1 week. (c) Comparison of the slip areas of the two M_w5.9 events. Blue and red represent the 2011 and 2016 events, respectively. The colored circles represent the ratio $s_{2011}/(s_{2011} + s_{2016})$, where s_{2011} and s_{2016} are the slip amounts of the 2011 and 2016 earthquakes, respectively, as shown in the color scale. Dots indicate the subfaults whose slip amounts are shown in Figure S15 in Supporting Information S1. (d) and (e): Moment-rate functions for the 2011 and 2016 events, respectively.

the slightly larger velocity and acceleration amplitudes observed at the nearest stations (Figures 2c and 2d). The moment-scaled radiated energies based on the obtained seismic moments are $e_R = \frac{E_R}{M_0} = 1.57 \times 10^{-5}$ for the 2011 event and 1.19×10^{-5} for the 2016 event. These values are similar to or slightly smaller than the average value of 3×10^{-5} in the crust of Japan (Kanamori et al., 2020; Yoshida & Kanamori, 2023). Assuming a rigidity μ of 32 GPa, the radiation efficiencies are $\eta = 2\mu \frac{e_R}{\Delta\sigma_E} = 0.33$ for the 2011 event and 0.40 for the 2016 event. These values fall within the typical range (0.25–1.0) obtained for various tectonics worldwide (Venkataraman & Kanamori, 2004).

Both events had their main slips near the hypocenter of the 2011 event and away from the hypocenter of the 2016 event (Figure 9). The lateral extents of the main slip regions are similar for both events and align closely with the regions where gaps were observed in the early aftershock distributions (Figure 4). The moment-rate functions (Figures 9d and 9e) show that the 2011 event completed rupture in the first 5 s, whereas the 2016 event started the main rupture at $t = 5$ s and lasted approximately 5 s. Figure 10 shows the time variation of the slip distributions of the two events in six time windows (0.0–1.5, 1.5–3.0, 3.0–4.5, 4.5–6.0, 6.0–7.5, and 7.5–9.0 s). During the 2011 event, large slip occurred near the hypocenter at $t = 0.0$–1.5s. In contrast, the main slip of the 2016 event occurred approximately 5 km north of its hypocenter near the hypocenter of the 2011 event, approximately 5.0 s later (Figures 10j and 10k).

Figure 9c compares the final slip distributions of the two events on the map. We also calculated the slip ratio between the two events, $R(\boldsymbol{x})$, for each subfault and presented it in the figure, where $R(\boldsymbol{x}) = s_{2011}(x)/(s_{2011}(\boldsymbol{x}) + s_{2016}(\boldsymbol{x}))$, and $s_{2011}(\boldsymbol{x})$ and $s_{2016}(\boldsymbol{x})$ indicate the slip distribution of the 2011 and 2016 events, respectively. When $R(\boldsymbol{x})$ is close to 0.5, both events cause the same amount of slip on that subfault, while when $R(\boldsymbol{x})$ is close to 0 and 1, the slip occurs primarily only during the 2011 and 2016 events, respectively. To emphasize the subfaults with significant slip, results were excluded when the slip amounts for both events were less than 30 cm. The figure shows that one of the slip areas, located east of the 2011 hypocenter at depths

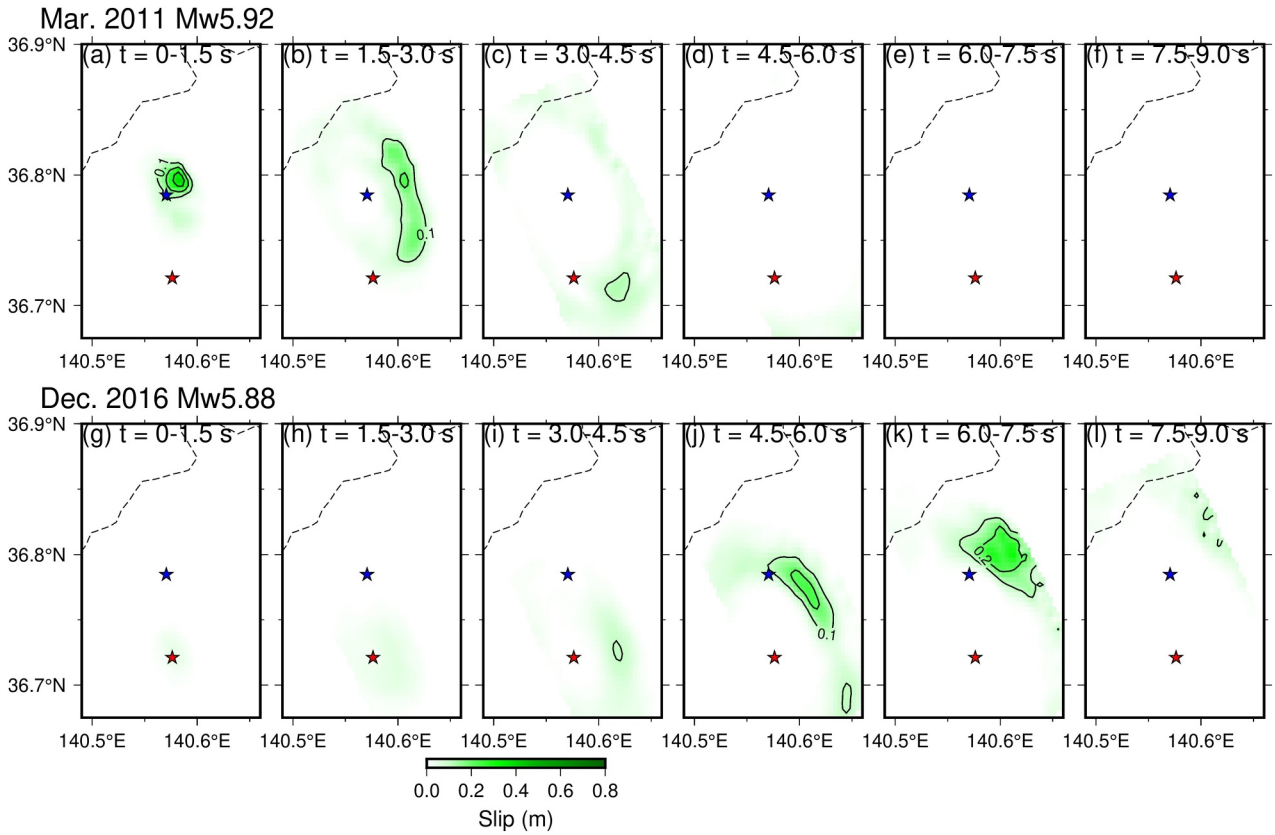

Figure 10. Time evolution of the coseismic slip distribution for the 2011 and 2016 M_w5.9 events. The amount of slip shown by color and contour represents the cumulative amount within each time window. The blue and red stars represent the 2011 and 2016 M_w5.9 epicenters, respectively.

shallower than 3 km, is nearly identical for both event (indicated by white circles; $R(\boldsymbol{x}) \sim 0.5$). This similarity explains the similar observed surface displacements (Figure 8). We refer to this area as the shallow slip area. In contrast, the slip areas on the deeper side ($3 < z < 6$ km) of the two earthquakes were offset, yet remained adjacent to each other. The largest slip area of the 2011 event is located just northeast of the hypocenter (blue star), while the peak of the 2016 slip is shifted to the southeast of the 2011 peak. We refer to these areas as the deep slip areas.

In general, the inversion results of the rupture process are subject to uncertainties. The uncertainties in the final slip distributions were examined by changing the three assumed parameters (V_r/V_s, t_h, and r_{wt}). Figure 11 shows the slip distributions of all the models whose VR_{mean}, VR_{wv}, and VR_{InSAR} were greater than 90% of those of the optimal model (shown by crosses in Figure S4 in Supporting Information S1 for $r_{wt} = 1.0$). The results indicated that the slip areas of the two events were fairly stably determined (Figure 11). The two deep slip areas are offset in all cases, while the shallow slip areas consistently overlap for both events. Overall, our slip distribution exhibits more localized slip areas compared to those of Fukushima et al. (2018), due to the enhanced spatial resolution provided by the waveform data.

Yoshida et al. (2024a) estimated the depth variation in the Q-value in this region and suggested that the Q-value is significantly smaller (~55) than that assumed in the shallow part ($z < 3$ km), affecting the high-frequency waveforms (>15 Hz). We performed an inversion using Green's function with the shallow low Q-value model and obtained results that were nearly identical to the original (Figure S6 in Supporting Information S1). Because we used near-source data, the effect of the low Q-value was negligible in this low-frequency band (<1 Hz).

Above, we used a simple single-fault model. However, the spatial pattern in the InSAR records suggests that the fault strike may change just south of the displacement peak (Fukushima et al., 2018). Building on this idea, we also created a fault model consisting of two planar faults with different strike and dip angles and performed additional inversions using the same data. Following Hikima (2023), we assumed a 141° strike and 47° dip for the northern fault, and a 160° strike and 50° dip for the southern fault (Figure 7 and Figure S7 in Supporting

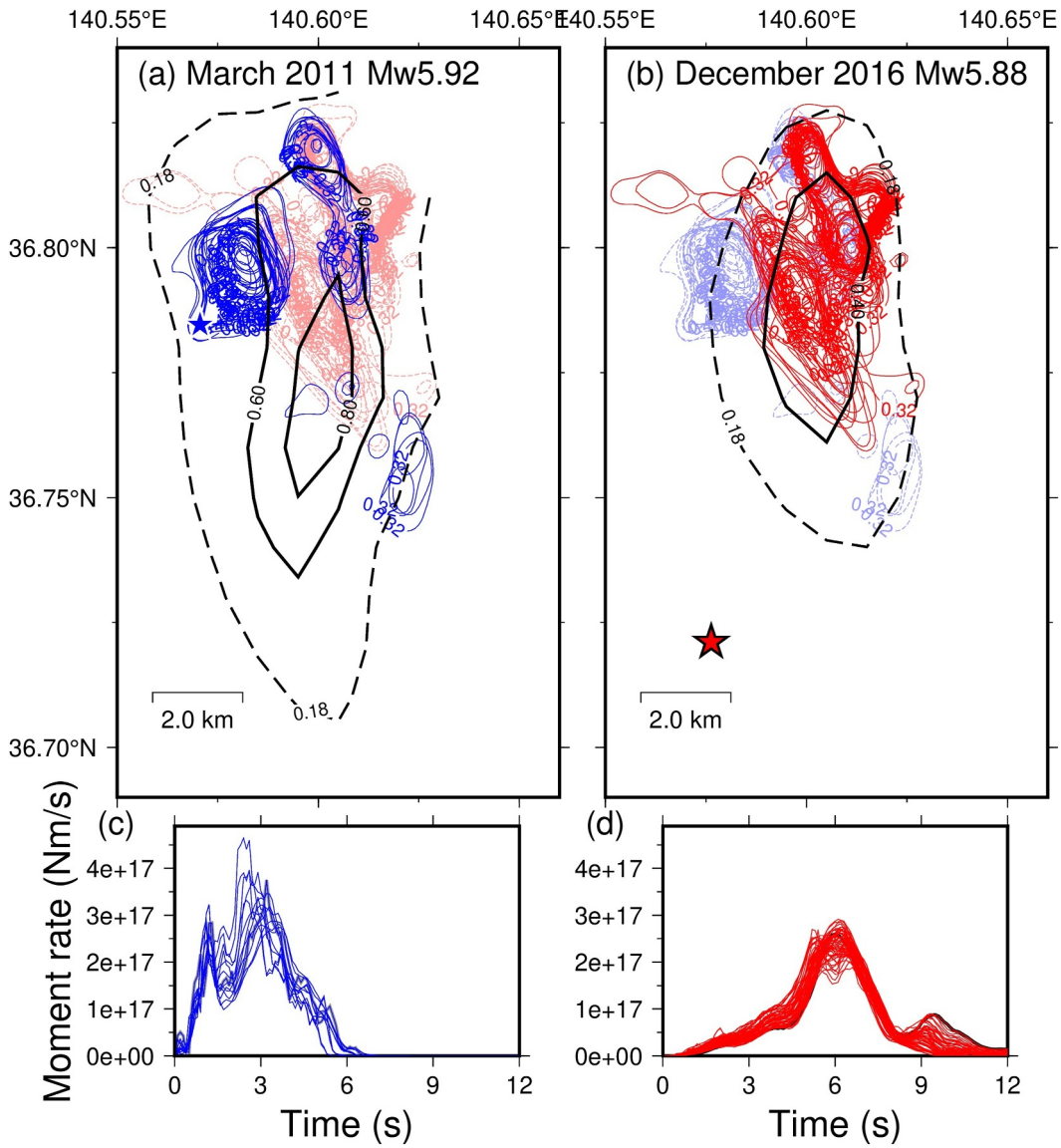

Figure 11. Variation of results for different assumed parameters. (a): The 2011 event; (b) the 2016 event. The light-colored contour represents the slip amount of the other event. Blue and red stars represent the epicenters of the 2011 and 2016 M_w5.9 earthquakes, respectively. Black contour lines represent slip areas by Fukushima et al. (2018). (c) and (d): Moment-rate functions for the 2011 and 2016 events, respectively.

Information S1). The hypocenters of the 2011 and 2016 events are located on subfaults of the northern and southern faults, respectively. The width and length of each subfault are set to 1.1 and 0.7 km, respectively, resulting in a total of 403 subfaults. The rupture initiation time at each subfault is given by $t_{\text{front}} = r/v_r$, where r denotes the distance from the hypocenter to the center of the subfault. This result (Figure S7 in Supporting Information S1) also shares the same characteristics as our single planar fault model, with comparable variance reductions of 89% for the 2011 event and 88% for the 2016 event. In both results, the deeper slip areas are displaced from each other, while the shallower slip areas overlap. The locations of the deep slip areas for the 2011 and 2016 events are nearly identical to our single fault-model results, with the 2011 event associated with the northern fault and the 2016 event with the southern fault.

To evaluate the seismic constraints independently from the InSAR constraints, we performed inversions using only seismic waveform data (Figure S8 in Supporting Information S1). Estimating the slip distribution based on seismic waveforms alone depends on the assumption of rupture propagation. However, in the present case,

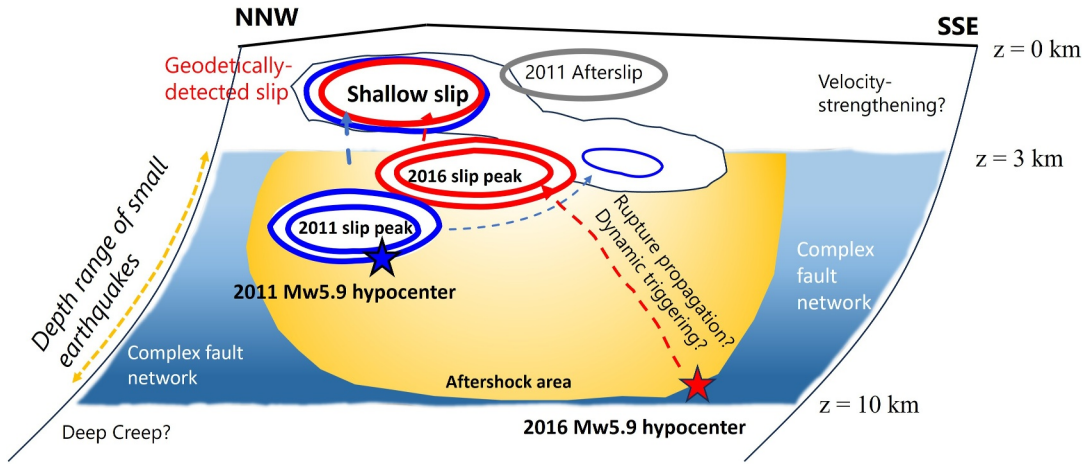

Figure 12. Schematic figure of the coseismic slip distributions of the two M_w5.9 events. Blue and red symbols indicate the 2011 and 2016 events, respectively. The stars represent the hypocenters, while the contour lines represent the main slip regions.

because near-field seismic waveform data, including surface displacement signals, are available (Figures 2c and 2d), the static slip distribution is expected to be robustly constrained. Indeed, the obtained slip models are similar to our joint inversion results at depths greater than 3 km (Figure S8 in Supporting Information S1). Waveform fitting is slightly better than for joint inversion, with VR_{wv} of 88.0% and 86.8% for the 2011 and 2016 events, respectively, though the difference is minimal. They also roughly reproduced the surface displacements (Figure S9 in Supporting Information S1; VR_{InSAR} = 54% for the 2011 event and VR_{InSAR} = 66% for the 2016 event). In the case of the 2016 event, the inversion using waveform alone effectively reproduces the peak of the InSAR displacement. However, the amount of shallow slip is too small for the 2011 event and does not explain the large local surface displacement near the shallow ends of the faults. This result indicates that, even when near-source seismic waveform data are available, the combined use of InSAR data is necessary to fully resolve shallow slip.

Because the main rupture of the 2016 event occurred away from the hypocenter, it is possible that the ruptures at the hypocenter and the main slip area represent separate events. To test this hypothesis, we consider a scenario in which the 2016 event was initiated at the same hypocenter as the 2011 event. We set the delay time to 4.0 s after the onset, based on Figure 9e, and performed the same joint inversion with various parameters of V_r/V_s and t_h. The maximum VR_{mean} is 89.0% (VR_{wv} = 84.6% and VR_{InSAR} = 93.4%) when V_r/V_s = 0.9 and t_h = 0.3 (Figures S1, S11, and S12 in Supporting Information S1). This value is comparable to the VR_{mean} for the original setting (89.3%). Even in this case, the deep slip patch of the 2016 event is complementary and shallower than that of the 2011 event (Figures S10 and S11 in Supporting Information S1), similar to the original results.

5. Discussion

The two M_w5.9 events occurring 5.8 years apart in northern Ibaraki Prefecture have been characterized by near-identical surface displacement patterns and widely different seismic waveforms. Previous studies have used two types of data separately and obtained different trends. This study performed a joint inversion and reconciled near-identical surface displacements with different waveforms.

Figure 12 summarizes the results. The hypocenters of the two events are offset by approximately 10 km (Figure 3), and the rupture processes of the two events are markedly different and are responsible for their widely different seismic waveforms (Figure 3). In the 2016 event, the main rupture occurred nearly 10 km from the hypocenter and might have been dynamically triggered by seismic waves rather than by rupture propagation initiated at the hypocenter. Nevertheless, the main slip areas of the two events were close to each other. The inferred deep slip areas (z > 3 km) of the two events are adjacent to each other (Figure 9). Aftershocks are distributed in a manner that avoids these areas, likely reflecting stress redistribution.

Based on similar InSAR images, previous geodetic studies have suggested that the two events caused repeated ruptures at the same segment on the same fault (Fukushima et al., 2018; Wimpenny et al., 2022). Short-term repetition of events as large as $M_w \sim 6$ has occasionally been reported at plate boundaries (e.g., Yoshida, 2023), although they are rare on intraplate faults. However, our results suggest that the 2011 and 2016 earthquakes were not repeating earthquakes. Tests with different rupture parameters always resulted in an offset in the deep slip areas for the two events (Figure 11). Based on surface displacement data, Wimpenny et al. (2022) showed that the amount of interseismic stress increase between the two events was insufficient for the 2016 event to re-rupture the 2011 event rupture area. A stress drop >5 MPa in the deep slip area of the 2011 event (Figure S5 in Supporting Information S1) also suggests that slip repetition in this area does not occur easily.

The obtained feature of the deep slip area of the 2011 event, adjacent to that of the 2016 event, is consistent with previous studies based on seismic waveform data (Hikima, 2023; Tanaka & Iwakiri, 2017). However, the previous models did not explain the near-identical surface displacements obtained from InSAR observations. Our joint inversion results include areas of relatively high slip at shallower depths ($z < 3$ km), which explain the short-wavelength pattern of the surface displacement near the top of the fault. Over 30 cm of coseismic slip occurred at the shallow depth ($z < 3$ km). The moment releases at $z < 3$ km are approximately 35% and 39% of the total moment releases for the 2011 and 2016 events, respectively. The depth profiles of the slip near the major slip area (indicated by dots in Figure 9c) show that the cumulative slip from both earthquakes remains approximately constant at about 0.9 m, within depths ranging from 1 to 3 km (Figure S13 in Supporting Information S1). This value is somewhat smaller than, but comparable to, the 1.1 m slip at the peak located at a depth of 4.5 km.

Figure 13 shows the distribution of surface displacements calculated from the subfaults at $z < 3$ km (Figures 13a and 13b) and $z > 3$ km (Figures 13c and 13d). The deep slip at $z > 3$ km contributes to the overall long-wavelength pattern, and the major influence on the observed local displacement is the shallow slip at $z < 3$ km. In contrast, for the waveforms, shallow slip ($z < 3$ km) has only a minor effect on the later portions of the waveforms (Figure S3 in Supporting Information S1). Thus, shallow slip areas were not imaged for the 2011 event only from seismic waveform data, even with near-field data. Nevertheless, the contribution of shallow slip is crucial for surface displacements.

Our results show that a slight difference in the deep slip area can produce near-identical InSAR image patterns if the shallow slip areas are close (Figure 8). This implies that similar surface displacement patterns can arise even when the major slip areas at depth are not indentical. This nonuniqueness in fault slip inversions is widely known, and our results highlight that this problem exists even for shallow ($z < 10$ km) surface-rupturing events because of the strong shallow-depth sensitivity of the surface displacement data. Combining surface displacement and seismic waveform data is essential for unraveling the details of the rupture processes for shallow earthquakes.

Our InSAR data for the 2011 event were derived from the radar image acquired one day after the event (Fukushima et al., 2018). We assumed that no significant afterslip occurred within a day, but several studies of other earthquakes have shown that early afterslips within a day can account for approximately 30% of the coseismic slip (Jiang et al., 2021; Milliner et al., 2020). Differences in observation timescales can be problematic when using seismic and geodetic data jointly for fault slip inversions. In our study, because the slip at the shallowest part ($z < 3$ km) is not constrained by the seismic waveforms (Figure S8 in Supporting Information S1), we may not completely eliminate the possibility that the shallowest slip occurred as extremely early afterslip within a day. However, InSAR images obtained by Wimpenny et al. (2022) (Figure 4 in Wimpenny et al., 2022) suggest that at least a few days following the mainshock, afterslip did not occur in the area where our joint inversion estimated shallow slip but to the south of it.

For the 2016 event, our InSAR data were derived from the radar image acquired 56 days after the event (Fukushima et al., 2018). According to Fukushima et al. (2018) and Wimpenny et al. (2022), the afterslip of the 2016 event is much smaller than that of the 2011 event, although some effects may still be present in the data because of the long time period. For the 2016 event, records from one day after the mainshock are also available for descending orbits (azimuth of 79.6° and incidence angle of 36.1°), despite the different LOS direction from that used for the 2011 event (Fukushima et al., 2018). We performed a source inversion of the 2016 event using the InSAR data from the descending LOS, with the same waveform data. The results are very similar to those obtained from the ascending record (Figures S14 and S15 in Supporting Information S1). In addition, this shallow area was also identified in the inversion results using only the waveform data (Figure S8b in Supporting Information S1), suggesting that the effect of aftershock slip is only minor.

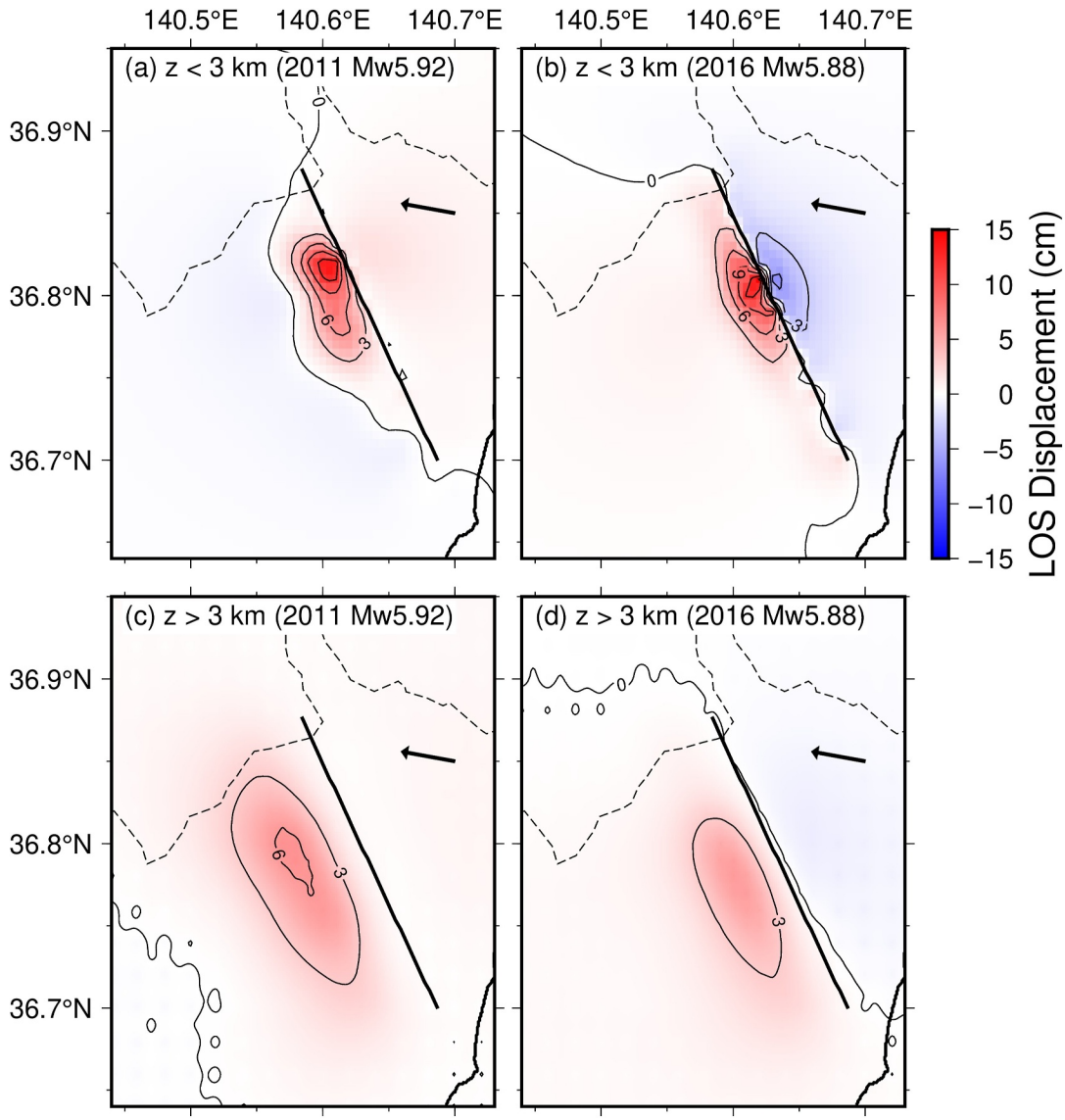

Figure 13. Surface displacements produced by shallow ($z < 3$ km) and deep ($z > 3$ km) subfaults. (a) and (b): Contributions of shallow subfaults ($z < 3$ km) to the surface displacements associated with the 2011 and 2016 events, respectively. (c) and (d): Contributions of deep subfaults ($z > 3$ km) to the surface displacements associated with the 2011 and 2016 events, respectively.

Our results suggest that the two mainshocks caused slip shallower than 3 km, contributing to localized surface displacement. Most aftershocks occurred at depths greater than 3 km (Figure 7), with almost no aftershocks shallower than 3 km near the mainshock rupture areas nor along the strike extension. The lack of small earthquakes suggests that the shallowest part ($z < 3$ km) of the fault can release the accumulated strain aseismically because of mildly velocity-strengthening (Kaneko et al., 2010) or conditionally stable velocity-weakening regimes due to small normal stresses at shallow depths (Scholz, 1998). Granite is distributed near the ground surface in this region (AIST Geological Survey of Japan, 2023). The temperature dependence of the frictional properties of granite (Blanpied et al., 1991) or clay evolution on the faut (Vrolijk & van der Pluijm, 1999) may have contributed to the development of the velocity-strengthening frictional properties. Nevertheless, the coseismic ruptures may have propagated through this aseismic segment during the two events, possibly due to their dynamic stress changes (e.g., Kaneko et al., 2008), and caused shallow slip that significantly contributed to the surface displacement.

The deep slip in 2016 occurred at a depth of 3–4 km, near the depth where smaller events cease to occur at shallower levels. The 2011 event did not cause significant slip in the 2016 deep patch, suggesting that this slip patch acted as a barrier during the 2011 event due to a local geometrical bump or fault bend. Following the 2011 M_w5.9 event, its significant afterslip, postseismic deformation of the Tohoku earthquake (Fukushima et al., 2018; Wimpenny et al., 2022), and other small earthquakes may have accumulated shear stresses in this patch, ultimately causing it to rupture and produce a large slip during the 2016 event. The deep slip patches of the 2016 and 2011 events exhibit velocity-weakening, rather than velocity-strengthening, frictional behavior. This situation for the intraplate fault may be analogous to the prevailing type of asperity model based on the rate-and state-dependent friction laws (Dieterch, 1979; Ruina, 1983), where the velocity-strengthening zone surrounds the seismic asperities.

The slip models for the 2011 and 2016 events presented in this study offer valuable insights into the physical processes driving the seismic cycle of the intraplate fault. However, further investigation is necessary, particularly to quantify the static and dynamic stress interactions between the inferred shallow and deep fault-slip patches. Such analyses are essential for a more comprehensive understanding of the earthquake cycle on the intraplate fault, especially under the influence of time-dependent loading associated with the 2011 Tohoku earthquake.

6. Conclusion

We complemented previous geodetic data with near-field seismic waveform data to enhance the spatial resolution of two near-identical M_w5.9 earthquakes in northern Ibaraki Prefecture, Japan. The results showed that the deep slip areas ($3 < z < 6$ km) of the two events are adjacent to each other and that they were not repeated ruptures of the same slip patch. Nevertheless, the observed InSAR data were very similar because the shallowest slip areas ($z < 3$ km) largely overlapped. Seismic waveforms are typically less sensitive to late slips during the rupture process, and surface displacements have a lower spatial resolution for deeper slips. These differences indicate that seismic waveform and surface displacement data should be jointly used to unravel the detailed processes of shallow events ($z < 10$ km). Small earthquakes rarely occur at depths shallower than 3 km in this region, suggesting that the shallow segment can release accumulated strain aseismically. The two mainshock ruptures may have triggered aseismic slip in the same aseismic segment, possibly due to the dynamic stress changes, producing characteristic surface displacements.

Data Availability Statement

The InSAR data used in this study and the slip inversion results are available at Zenodo via https://doi.org/10.5281/zenodo.14772367 with CC-BY 4.0 license (Yoshida et al., 2025). The seismograms used in this study were collected and stored by the JMA, national universities, and the National Research Institute for Earth Science and Disaster Resilience (NIED, 2019). This study used the hypocenter catalog by Yoshida et al. (2024b) and moment tensor data from the F-net moment tensor catalog (Kubo et al., 2002). The figures were created using the Generic Mapping Tool (GMT; Wessel & Smith, 1998).

Acknowledgments
We thank Blandine Gardonio and an anonymous reviewer for their valuable suggestions. We also would like to thank the Editor (Satoshi Ide) and the Associate Editor (Anne Socquet) for handling the manuscript and for their support throughout the process. This study was financially supported by the JSPS KAKENHI (Grants 20K14569, 24H01017, and 21H05206).

References

AIST, Geological Survey of Japan. (2023). Seamless digital geological map of Japan V2 1:200,000, Legend 400 edition. Retrieved from https://gbank.gsj.jp/seamless/

Blanpied, M. L., Lockner, D. A., & Byerlee, J. D. (1991). Fault stability inferred from granite sliding experiments at hydrothermal conditions. *Geophysical Research Letters*, *18*(4), 609–612. https://doi.org/10.1029/91GL00469

Bourouis, S., & Bernard, P. (2007). Evidence for coupled seismic and aseismic fault slip during water injection in the geothermal site of Soultz (France), and implications for seismogenic transients. *Geophysical Journal International*, *169*(2), 723–732. https://doi.org/10.1111/j.1365-246x.2006.03325.x

Brune, J. N. (1970). Tectonic stress and the spectra of seismic shear waves from earthquakes. *Journal of Geophysical Research*, *75*(26), 4997–5009. https://doi.org/10.1029/jb075i026p04997

Dieterich, J. H. (1979). Modeling of rock friction: 1. Experimental results and constitutive equations. *Journal of Geophysical Research*, *84*(B5), 2161–2168. https://doi.org/10.1029/JB084iB05p02161

Dreger, D. S., Huang, M., Rodgers, A., Taira, T., & Wooddell, K. (2015). Kinematic finite-source model for the 24 August 2014 South Napa, California, earthquake from joint inversion of seismic, GPS, and InSAR data. *Seismological Research Letters*, *86*(2A), 327–334. https://doi.org/10.1785/0220140244

Eshelby, J. D. (1957). The determination of the elastic field of an ellipsoidal inclusion, and related problems. *Proceedings of the Royal Society of London. Series A. Mathematical and Physical Sciences*, *241*(1226), 376–396.

Fukushima, Y., Toda, S., Miura, S., Ishimura, D., Fukuda, J., Demachi, T., & Tachibana, K. (2018). Extremely early recurrence of intraplate fault rupture following the Tohoku-Oki earthquake. *Nature Geoscience*, *11*(10), 777–781. https://doi.org/10.1038/s41561-018-0201-x

Funning, G. J., Fukahata, Y., Yagi, Y., & Parsons, B. (2014). A method for the joint inversion of geodetic and seismic waveform data using ABIC: Application to the 1997 Manyi, Tibet, earthquake. *Geophysical Journal International*, *196*(3), 1564–1579. https://doi.org/10.1093/gji/ggt406

Hartzell, S. H., & Heaton, T. H. (1983). Inversion of strong ground motion and teleseismic waveform data for the fault rupture history of the 1979 Imperial Valley, California, earthquake. *Bulletin of the Seismological Society of America*, *73*(6), 1553–1583. https://doi.org/10.1785/bssa07306a1553

Hayashi, M., & Hiramatsu, Y. (2013). Spatial distribution of similar aftershocks of a large inland earthquake, the 2000 Western Tottori earthquake, in Japan. *Earth Planets and Space*, *65*(12), 1587–1592. https://doi.org/10.5047/eps.2013.09.002

Hikima, K. (2023). Distinct rupture processes on a fault where M6-class earthquakes reoccurred in a short period: Analysis of the 2011 and 2016 Northern Ibaraki, Japan, earthquakes using near-field waveforms. *Earth Planets and Space*, *75*(1), 169. https://doi.org/10.1186/s40623-023-01928-y

Hiramatsu, Y., Hayashi, M., & Hayashi, A. (2011). Relation between similar aftershocks and ruptured asperity of a large inland earthquake: Example of the 2007 Noto Hanto earthquake. *Earth Planets and Space*, *63*(2), 145–149. https://doi.org/10.5047/eps.2010.11.010

Iio, Y., & Kobayashi, Y. (2002). A physical understanding of large intraplate earthquakes. *Earth Planets and Space*, *54*(11), 1001–1004. https://doi.org/10.1186/BF03353292

Imanishi, K., Ando, R., & Kuwahara, Y. (2012). Unusual shallow normal-faulting earthquake sequence in compressional northeast Japan activated after the 2011 off the Pacific coast of Tohoku earthquake. *Geophysical Research Letters*, *39*(9), L09306. https://doi.org/10.1029/2012GL051491

Jiang, J., Bock, Y., & Klein, E. (2021). Coevolving early afterslip and aftershock signatures of a San Andreas fault rupture. *Science Advances*, *7*(15), eabc1606. https://doi.org/10.1126/sciadv.abc1606

Kanamori, H., Ross, Z. E., & Rivera, L. (2020). Estimation of radiated energy using the KiK-net downhole records—Old method for modern data. *Geophysical Journal International*, *221*(2), 1029–1042. https://doi.org/10.1093/gji/ggaa040

Kaneko, Y., Avouac, J.-P., & Lapusta, N. (2010). Towards inferring earthquake patterns from geodetic observations of interseismic coupling. *Nature Geoscience*, *3*(5), 363–369. https://doi.org/10.1038/ngeo843

Kaneko, Y., Lapusta, N., & Ampuero, J.-P. (2008). Spectral element modeling of spontaneous earthquake rupture on rate and state faults: Effect of velocity-strengthening friction at shallow depths. *Journal of Geophysical Research*, *113*(B9), B09317. https://doi.org/10.1029/2007jb005553

Kato, A., Sakai, S., & Obara, K. (2011). A normal-faulting seismic sequence triggered by the 2011 off the Pacific coast of Tohoku Earthquake: Wholesale stress regime changes in the upper plate. *Earth Planets and Space*, *63*(7), 745–748. https://doi.org/10.5047/eps.2011.06.014

Kim, A., Dreger, D. S., Taira, T., & Nadeau, R. M. (2016). Changes in repeating earthquake slip behavior following the 2004 Parkfield main shock from waveform empirical Green's functions finite-source inversion. *Journal of Geophysical Research: Solid Earth*, *121*(3), 1910–1926. https://doi.org/10.1002/2015jb012562

Kubo, A., Fukuyama, E., Kawai, H., & Nonomura, K. (2002). NIED seismic moment tensor catalogue for regional earthquakes around Japan: Quality test and application. *Tectonophysics*, *356*(1–3), 23–48. https://doi.org/10.1016/S0040-1951(02)00375-X

Kubo, H., Asano, K., & Iwata, T. (2013). Source-rupture process of the 2011 Ibaraki-Oki, Japan, earthquake (M_w 7.9) estimated from the joint inversion of strong-motion and GPS Data: Relationship with seamount and Philippine Sea Plate. *Geophysical Research Letters*, *40*(12), 3003–3007. https://doi.org/10.1002/grl.50558

Kubota, T., Saito, T., & Hino, R. (2022). A new mechanical perspective on a shallow megathrust near-trench slip from the high-resolution fault model of the 2011 Tohoku-Oki earthquake. *Progress in Earth and Planetary Science*, *9*(1), 68. https://doi.org/10.1186/s40645-022-00524-0

Lawson, C. L., & Hanson, R. J. (1995). Solving least squares problems. *Journal of the American Statistical Association*, *72*(360), 930. https://doi.org/10.2307/2286501

Lay, T., & Kanamori, H. (1981). An asperity model of large earthquake sequences. *Earthquake Prediction: An International Review*, 579–592. https://doi.org/10.1029/me004p0579

Lengliné, O., Lamourette, L., Vivin, L., Cuenot, N., & Schmittbuhl, J. (2014). Fluid-induced earthquakes with variable stress drop. *Journal of Geophysical Research: Solid Earth*, *119*(12), 8900–8913. https://doi.org/10.1002/2014jb011282

Lin, Y. Y., Ma, K. F., Kanamori, H., Alex Song, T. R., Lapusta, N., & Tsai, V. C. (2016). Evidence for non-self-similarity of microearthquakes recorded at a Taiwan borehole seismometer array. *Geophysical Journal International*, *206*(2), 757–773. https://doi.org/10.1093/gji/ggw172

Magen, Y., Inbal, A., Ziv, A., Baer, B., Bürgmann, R., Periollat, A., & Sagiya, T. (2024). The Elusive role of aseismic slip along a Seaward dipping normal fault in the indirect triggering of a Normal Faulting earthquake sequence in Northeast Japan following the 2011 Tohoku-Oki Megathrust. *Journal of Geophysical Research: Solid Earth*, *129*(8), e2024JB028903. https://doi.org/10.1029/2024JB028903

Matsuzawa, T., Igarashi, T., & Hasegawa, A. (2002). Characteristic small-earthquake sequence off Sanriku, northeastern Honshu, Japan. *Geophysical Research Letters*, *29*(11), 1543. https://doi.org/10.1029/2001GL014632

Meneses-Gutierrez, A., & Nishimura, T. (2020). Inelastic deformation zone in the lower crust for the San-in Shear Zone, Southwest Japan, as observed by a dense GNSS network. *Earth Planets and Space*, *72*(1), 10. https://doi.org/10.1186/s40623-020-1138-z

Milliner, C., Bürgmann, R., Inbal, A., Wang, T., & Liang, C. (2020). Resolving the kinematics and moment release of early afterslip within the first hours following the 2016 Mw 7.1 Kumamoto earthquake: Implications for the shallow slip deficit and frictional behavior of aseismic creep. *Journal of Geophysical Research: Solid Earth*, *125*(9), e2019JB018928. https://doi.org/10.1029/2019jb018928

Nadeau, R. M., & Johnson, L. R. (1998). Seismological studies at parkfield VI: Moment release rates and estimates of source parameters for small repeating earthquakes. *Bulletin of the Seismological Society of America*, *88*(3), 790–814. https://doi.org/10.1785/bssa0880030790

Nakajima, J., & Hasegawa, A. (2023). Prevalence of repeating earthquakes in the continental crust and subducting slabs: Triggering of earthquakes by aseismic slip. *Journal of Geophysical Research: Solid Earth*, *128*(2), e2022JB024667. https://doi.org/10.1029/2022jb024667

Naoi, M., Nakatani, M., Igarashi, T., Otsuki, K., Yabe, Y., Kgarume, T., et al. (2015). Unexpectedly frequent occurrence of very small repeating earthquakes ($-5.1 \leq M_w \leq -3.6$) in a South African gold mine: Implications for monitoring intraplate faults. *Journal of Geophysical Research: Solid Earth*, *120*(12), 8478–8493. https://doi.org/10.1002/2015JB012447

NIED. (2019). NIED K-net, KiK-net [Dataset]. *National Research Institute for Earth Science and Disaster Resilience*. https://doi.org/10.17598/NIED.0004

Noda, A., Saito, T., & Fukuyama, E. (2018). Slip-deficit rate distribution along the Nankai Trough, Southwest Japan, with elastic lithosphere and viscoelastic asthenosphere. *Journal of Geophysical Research: Solid Earth*, *123*(9), 8125–8142. https://doi.org/10.1029/2018jb015515

Noda, H., Lapusta, N., & Kanamori, H. (2013). Comparison of average stress drop measures for ruptures with heterogeneous stress change and implications for earthquake physics. *Geophysical Journal International*, *193*(3), 1691–1712. https://doi.org/10.1093/gji/ggt074

Okada, Y. (1992). Internal deformation due to shear and tensile faults in a half-space. *Bulletin of the Seismological Society of America*, *82*(2), 1018–1040. https://doi.org/10.1785/bssa0820021018

Ruina, A. (1983). Slip instability and state variable friction laws. *Journal of Geophysical Research*, *88*(B12), 10359–10370. https://doi.org/10.1029/JB088iB12p10359

Ryder, I., & Bürgmann, R. (2008). Spatial variations in slip deficit on the central San Andreas Fault from InSAR. *Geophysical Journal International*, *175*(3), 837–852. https://doi.org/10.1111/j.1365-246x.2008.03938.x

Saito, T., & Noda, A. (2022). Mechanically coupled areas on the plate interface in the nankai trough, Japan and a possible seismic and aseismic rupture scenario for megathrust earthquakes. *Journal of Geophysical Research: Solid Earth*, *127*(8), e2022JB023992. https://doi.org/10.1029/2022jb023992

Savage, J. (1983). A dislocation model of strain accumulation and release at a subduction zone. *Journal of Geophysical Research*, *88*(3), 4984–4996. https://doi.org/10.1029/jb088ib06p04984

Scholz, C. H. (1998). Earthquakes and friction laws. *Nature*, *391*(6662), 37–42. https://doi.org/10.1038/34097

Suwa, Y., Miura, S., Hasegawa, A., Sato, T., & Tachibana, K. (2006). Interplate coupling beneath NE Japan inferred from three-dimensional displacement field. *Journal of Geophysical Research*, *111*(4), 1–12. https://doi.org/10.1029/2004JB003203

Tanaka, M., & Iwakiri, K. (2017). Source rupture processes of earthquakes in Northern Ibaraki prefecture (MJMA6.1, MJMA6.3) and Comparison between the rupture areas of the two earthquakes. *Journal of Seismology, Volcanology and Related Engineering*, *81*(7), 1–11.

Uchida, N. (2019). Detection of repeating earthquakes and their application in characterizing slow fault slip. *Progress in Earth and Planetary Science*, *6*(1), 1–21. https://doi.org/10.1186/s40645-019-0284-z

Uchida, N., & Bürgmann, R. (2019). Repeating earthquakes. *Annual Review of Earth and Planetary*, *47*(1), 305–332. https://doi.org/10.1146/annurev-earth-053018-060119

Venkataraman, A., & Kanamori, H. (2004). Observational constraints on the fracture energy of subduction zone earthquakes. *Journal of Geophysical Research*, *109*(5), B05302. https://doi.org/10.1029/2003JB002549

Vrolijk, P., & van der Pluijm, B. A. (1999). Clay gouge. *Journal of Structural Geology*, *21*(8–9), 1039–1048. https://doi.org/10.1016/s0191-8141(99)00103-0

Wald, D. J., & Heaton, T. H. (1994). Spatial and temporal distribution of slip for the 1992 Landers, California, earthquake. *Bulletin of the Seismological Society of America*, *84*(3), 668–691. https://doi.org/10.1785/bssa0840030668

Wessel, P., & Smith, W. H. F. (1998). New, improved version of generic mapping tools released [Software]. *Eos, Transactions American Geophysical Union*, *79*(47). 579. https://doi.org/10.1029/98EO00426

Wimpenny, S., Forrest, N., & Copley, A. (2022). Time-dependent decrease in fault strength in the 2011–2016 Ibaraki-Fukushima Earthquake sequence. *Geophysical Journal International*, *232*(2), 788–809. https://doi.org/10.1093/gji/ggac368

Yoshida, K. (2023). The M_w 6.0-6.8 quasi-repeating earthquakes off Miyagi, Japan, with variable moment release patterns due to a hidden adjacent slip patch. *Journal of Geophysical Research: Solid Earth*, *128*(2), e2022JB025654. https://doi.org/10.1029/2022jb025654

Yoshida, K. (2024). Direct evidence for diverse source complexity in small earthquakes (M_w 3.3–5.0) obtained from near-source borehole seismic data. *Seismological Research Letters*, *95*(4), 2409–2421. https://doi.org/10.1785/0220230431

Yoshida, K., Emoto, K., Takemura, S., & Matsuzawa, T. (2024a). Near-source waveform modeling to estimate shallow crustal attenuation and radiated energy of Mw 2.0-4.5 earthquakes. *Journal of Geophysical Research: Solid Earth*, *129*(9), e2023JB028523. https://doi.org/10.1029/2023JB028523

Yoshida, K., Emoto, K., Takemura, S., & Matsuzawa, T. (2024b). Hypocenters, focal mechanisms, and radiated energy of small earthquakes in Northern Ibaraki Prefecture, Japan [Dataset]. *Zenodo*. https://doi.org/10.5281/zenodo.11626608

Yoshida, K., Fukushima, Y., & Kaneko, Y. (2025). Joint inversion results and InSAR data for the 2011 and 2016 Mw5.9 Northern Ibaraki earthquakes [Dataset]. *Zenodo*. https://doi.org/10.5281/zenodo.14772367

Yoshida, K., Hasegawa, A., Noguchi, S., & Kasahara, K. (2020). Low-frequency earthquakes observed in close vicinity of repeating earthquakes in the brittle upper crust of Hakodate, Hokkaido, Northern Japan. *Geophysical Journal International*, *223*(3), 1724–1740. https://doi.org/10.1093/gji/ggaa418

Yoshida, K., Hasegawa, A., & Okada, T. (2015a). Spatial variation of stress orientations in NE Japan revealed by dense seismic observations. *Tectonophysics*, *647*, 63–72. https://doi.org/10.1016/j.tecto.2015.02.013

Yoshida, K., Hasegawa, A., & Okada, T. (2015b). Spatially heterogeneous stress field in the source area of the 2011 M_w6.6 Fukushima-Hamadori earthquake, NE Japan, probably caused by static stress change. *Geophysical Journal International*, *201*(2), 1062–1071. https://doi.org/10.1093/gji/ggv068

Yoshida, K., Hasegawa, A., Okada, T., Iinuma, T., Ito, Y., & Asano, Y. (2012). Stress before and after the 2011 great Tohoku-Oki earthquake and induced earthquakes in inland areas of eastern Japan. *Geophysical Research Letters*, *39*(3), L03302. https://doi.org/10.1029/2011GL049729

Yoshida, K., Hasegawa, A., Yoshida, T., & Matsuzawa, T. (2019). Heterogeneities in stress and strength in Tohoku and its relationship with earthquake sequences triggered by the 2011 M9 Tohoku-oki earthquake. *Pure and Applied Geophysics*, *176*(3), 1335–1355. https://doi.org/10.1007/s00024-018-2073-9

Yoshida, K., & Kanamori, H. (2023). Time-domain source parameter estimation of M_w 3–7 earthquakes in Japan from a large database of moment-rate functions. *Geophysical Journal International*, *234*(1), 243–262. https://doi.org/10.1093/gji/ggad068

Yoshida, K., Taira, T., Matsumoto, Y., Saito, T., Emoto, K., & Matsuzawa, T. (2020). Stress release process along an intraplate fault analogous to the plate boundary: A case study of the 2017 M5.2 akita-daisen earthquake, NE Japan. *Journal of Geophysical Research: Solid Earth*, *125*(5), e2020JB019527. https://doi.org/10.1029/2020JB019527

Yoshida, S., Koketsu, K., Shibazaki, B., Sagiya, T., Kato, T., & Yoshida, Y. (1996). Joint inversion of near-and far-field waveforms and geodetic data for the rupture process of the 1995 kobe earthquake. *Journal of Physics of the Earth*, *44*(5), 437–454. https://doi.org/10.4294/jpe1952.44.437

Yukutake, Y., Yoshida, K., & Honda, R. (2022). Interaction between aseismic slip and fluid invasion in earthquake swarms revealed by dense geodetic and seismic observations. *Journal of Geophysical Research: Solid Earth*, *127*(4), e2021JB022933. https://doi.org/10.1029/2021jb022933

Zhu, L., & Rivera, L. a. (2002). A note on the dynamic and static displacements from a point source in multilayered media. *Geophysical Journal International*, *148*(3), 619–627. https://doi.org/10.1046/j.1365-246X.2002.01610.x